Lab on a Chip

Antibody-functionalized aluminum oxide-coated particles targeting neutrophil receptors in a multifrequency microfluidic impedance cytometer

Journal:	*Lab on a Chip*
Manuscript ID	LC-ART-06-2022-000563
Article Type:	Paper
Date Submitted by the Author:	21-Jun-2022
Complete List of Authors:	Ashley, Brandon ; Rutgers University New Brunswick, Sui, Jinaye; Rutgers The State University of New Jersey Javanmard, Mehdi; Rutgers The State University of New Jersey Hassan, Umer; Rutgers The State University of New Jersey, Electrical and Computer Engineering

Lab on a Chip

PAPER

Antibody-functionalized aluminum oxide-coated particles targeting neutrophil receptors in a multifrequency microfluidic impedance cytometer†

Received 00th January 20xx,
Accepted 00th January 20xx

DOI: 10.1039/x0xx00000x

Brandon K. Ashley[a], Jianye Sui[b], Medhi Javanmard[ab], and Umer Hassan[*abc]

Personalized diagnostics of infectious diseases require monitoring disease progression due to their ever-changing physiological conditions and the multi-faceted organ system mechanisms involved in disease pathogenesis. In such instances, the recommended clinical strategies involve multiplex data collection from critical biomarkers related to patient's conditions along with longitudinal frequent patient monitoring. Numerous detection technologies exist both in research and commercial settings to monitor these conditions, however, they fail to provide biomarker multiplexing ability with design and data processing simplicity. For a recently conceived multiplexing biomarker modality, this work demonstrates, the use of electrically sensitive microparticles targeting and identifying membrane receptors on leukocytes using a single detection source, with a high potential for multiplexing greater than any existing impedance-based single-detection schemes. Here, polystyrene microparticles are coated with varying thicknesses of metal oxides, which generated quantifiable impedance shifts when exposed to a multifrequency electric fields depending on the metal oxide thickness. Using multifrequency impedance cytometry, these particles can be measured and differentiated rapidly across one coplanar electrode scheme. After surface-functionalizing particles with antibodies targeting CD11b and CD66b receptors, the particles are combined with isolated neutrophils to measure receptor expression. A combination of data analysis techniques including multivariate analysis, supervised machine learning, and unsupervised machine learning was able to accurately differentiate samples with up to 91% accuracy. This proof-of-concept study demonstrates the potential for these oxide-coated particles for enumerating specific leukocytes enabling multiplexing. Further, additional coating thicknesses or different metal oxide materials can enable a compendium of multiplexing targeting resource to be used to develop a high-multiplexing sensor for targeting membrane receptor expression.

1 Introduction

To quantify micro-nano biological entities, a plethora of technologies are currently available, each with unique advantages and sample preparation requirements. Depending on the biomarker, biological sample, and sensing modality; these technologies may provide robust single biomarker measurement or limited multiplexing ability for sample analysis. For example, fluorescence quantification through flow cytometry can characteristically quantify receptor expression on stained cells for up to 18 receptors at once with high specificity[1–3], but has difficulty measuring more receptors without exceedingly expensive equipment, highly optimized sample preparation, and more complicated data processing[4–7] requirements. Static microscopy can provide detailed visual assessments and can be coupled with other sensing modalities like fluorescence labeling,, but is limited in detection throughput and also requires more sophisticated equipment as measured entities reduce to submicron dimensions[7–9]. Newer techniques such as quantum dot targeting and surface-plasmon resonance can provide submicron biomarker identification, but still require complicated fabrication methods[10–12]. There lies a need for a detection scheme with simple manufacturing and data processing requirements which can target a multitude of species biomarkers at once.

Among different sensing modalities, impedance cytometry stands out as a revolutionary tool to directly or indirectly detect the presence of both microscopic and/or nanoscopic objects, obtaining electrical information of such species without sample destruction at high-throughputs[13,14]. It has many useful applications, from size referencing in particle fabrication[15–18], air and water quality reporting[19–23], and most notoriously in biological cell assessments and disease diagnostics[24–27]. While accurate, its main advantage may come from manufacturing scalability, an attractive feature for point-of-care environments[7,25,27–29]. Either label-free or with electrically sensitive targeting agents, its versatility is applied to many measurement scenarios. However, with its current state there is still a trade-off in discerning multiple species simultaneously

[a] Department of Biomedical Engineering, Rutgers, the State University of New Jersey, Piscataway, NJ, 08854, USA.
[b] Department of Electrical Engineering, Rutgers, the State University of New Jersey, Piscataway, NJ, 08854, USA.
[c] Global Health Institute, Rutgers, the State University of New Jersey, New Brunswick, NJ, 08901, USA.
† Footnotes relating to the title and/or authors should appear here.
Electronic Supplementary Information (ESI) available: [details of any supplementary information available should be included here]. See DOI: 10.1039/x0xx00000x

between accuracy and fast analysis. This has proven to be a pitfall for many stratifying complicated disease profiles such as sepsis, acute kidney injury, urinary tract infections, and liver dysfunction[7,30–32]; which requires multiplex biomarker measurements for personalized patient stratification.

Expression of membrane receptors on immune cells are precursors to inflammatory response in diseases such as sepsis. The earliest (most notably for neonatal sepsis)[33,34] two critical biomarkers include neutrophil receptors such as CD11b and CD66b. Both are elevated during inflammation but represent different mechanisms. Specifically, CD11b participates in cell adhesion and migration in the presence of CD18[35]. Contrastingly, CD66b (or CEACAM8) is involved in adhesion but also in altering neutrophil migration patterns at higher levels[36]. Both are currently measured using fluorescence labels or antibody-specific immunoassays and are promising new sepsis biomarkers[36,37]. They also are both frequently evaluated in chronic autoimmune conditions such as rheumatoid arthritis and lupus nephritis, as well as certain cancers[38–44].

For a novel multiplexing impedance cytometry mechanism to measure these receptors, this research uses microparticles semi-coated with metal oxides that produce unique signals when different voltage frequencies are carried in an electric field relative to impedance changes. These nanometer sized metal oxide layers can be differentiated both by the materials used for the metal oxide (e.g., Al_2O_3, HfO_2, TiO_2, etc.) and the metal oxide layer thickness varying from 5 to 30 nm, which can be identified through a 10 nm layer difference[45]. In this scheme, the particles will be detected through a microfluidic impedance cytometry construct. Fig. 1a and 1b illustrates this process, where the middle center electrode is stimulated with a multifrequency ($f_{1\text{-}4}$) voltage (V_{in}) and the surrounding grounded electrodes complete the modeled circuit and generates an electric field in the area above in the channel[25]. When the metal oxide-coated Janus particle (MOJP) enters the electric field, it displaces dielectric fluid, and its material properties change the system's impedance. The current output then changes, and after transimpedance amplification and conversion from current signal to voltage signal, a characteristic pulse is recorded. The two grounded electrodes are significant to produce a bipolar pulse when taking a differential signal between them, increasing signal amplitude retrieved from the same particle and improving the system's sensitivity by removing common mode noise. Each MOJP then has a specific amplitude shift at different output frequencies, which can be used to electrically identify the particles[46]. Based on the thickness of antibody-functionalized Janus particles (i.e., aluminum oxide-semi coated particles with CD11b and CD66b targeting surface-functionalized antibodies), characteristic impedance shifts across a multi-frequency voltage will occur. This translates to receptor identification when conjugated to neutrophils with one emission and detection source.

2 Experimental section

2.1 Materials

Streptavidin (SAv, > 11 U per mg), phosphate buffered saline (PBS, 1X and 10X, pH = 7.2), dimethyl sulfoxide (DMSO, ≥ 99.9% purity), biotin-4-fluorscein, Atto 655-biotin, Ficoll-Paque density gradient, (3-Amino-propyl)triethoxysilane (APTES), and Roswell Park Memorial Institute medium 1640 (RPMI) were purchased through Sigma Aldrich (St. Louis, MO, USA). Biotinylated anti-CD11b monoclonal mouse antibody (> 95% purity) was purchased through Thermo Fisher Scientific (Waltham, MA, USA). Biotinylated anti-CD66b was (>98% purity) was purchased through BioLegend (San Diego, CA, USA). A NE-300 syringe pump was purchased from Southpoint Surgical Supply (Coral Springs, FL, USA). A HF2LI lock-in amplifier and HF2TA current amplifier was purchased through Zurich Instruments (Zurich, SUI). Fluorescein isothiocyanate (FITC) labeled anti-CD66b monoclonal antibody was purchased from Fisher Scientific (Hampton, NH, USA). Phycoerythrin (PE) labeled anti-CD11b monoclonal antibody was purchased from VWR International (Radnor, PA, USA). Deidentified human blood was obtained from Robert Wood Johnson Medical Hospital (New Brunswick, NJ, USA) through an institutional review board (IRB) study (Pro2018002356). The Moxi Go II Flow Cytometer was purchased from Orflo Technologies (Ketchum, ID, USA). LabView software was purchased and installed through National Instruments (Austin, TX, USA). MATLAB version 2020B was purchased and installed through Mathworks (Natick, MA, USA).

2.2 Metal oxide-coated particle fabrication

The fabrication process for the MOJPs has been detailed extensively in previous reports [45,46]. Briefly, nanosphere lithography formed 3 μm polystyrene microparticles which are used as the particle core. 20 nm of gold is semi-deposited above the particles using electron-beam deposition, followed by semi-coating either 10 nm or 30 nm of Al_2O_3 above the gold layer using atomic layer deposition.

2.3 Microelectrode and microchannel fabrication

Protocols for microfabricating coplanar electrodes and PDMS microchannels have been described in previous articles[18]. Briefly, 250 nm of chromium followed by 750 nm of gold was sputtered above glass wafers exposed to UV light with electrode dimensions using photolithography, forming the gold electrodes (Fig. 1c). Microchannel architecture was rendered above silicon wafers after UV exposure as well. PDMS was cured over microchannel structures after APTES wafer treatment and cut out with formed embedded channel design. Channel and electrodes were bonded after O_2 plasma exposure, with aligned channel focusing regions between electrodes (Fig. 1b). Silver conductive epoxy then adhered the device to a printed circuit board (PCB) which facilitates lock-in amplifier connection and data recording (Fig 1a, 1c).

2.4 Signal Acquisition, processing, and sampling algorithm

Lyophilized SAv was reconstituted in 1X PBS, with vortexing for 10 seconds followed by ultrasonic agitation for 10 minutes. In parallel, 2 μL of SAv (0.1 mg/mL) was combined with both 200

μL of 30 nm aluminum oxide coated-Janus microparticle (30nm MOJPs) as well as 200 μL of 10 nm aluminum oxide coated-Janus microparticle (10nm MOJPs) solutions ($5.92x10^7$ particles/mL each) and incubated for 12 hours at 0˚C. Here, the incubation period allows for SAv adsorption and ensures high stability binding[47]. After, the solutions were centrifuged for 10 minutes at 10,000g to separate MOJPs from unbound SAv. After supernatant aspiration, the particle pellet underwent further purification steps to reduce unbound SAv. This included pellet resuspension through ultrasonic agitation, centrifugation, and supernatant removal again. Reducing unbound SAv is critical so it does not competitively bind with the biotinylated antibodies in subsequent steps.

Following SAv adsorption to MOJPs, 10 μL of biotinylated anti-CD66b antibody (1 mg/mL in 1X PBS) was mixed with the SAv-adsorbed 30 nm MOJPs solution while 10 μL of biotinylated anti-CD11b antibody (1 mg/mL in 1X PBS) was mixed with the SAv-adsorbed 10 nm MOJPs solution, and further incubated for 8 hours at 0˚C. Like SAv purification following incubation, the solution was washed with the same conditions and parameters to purify MOJPs and separate out unbound antibodies (i.e., centrifugation, supernatant aspiration, pellet resuspension in 1X PBS, etc.)[48].

2.5 Human blood samples acquisition

We collected human blood samples from Robert Wood Johnson Medical Hospital (RWJMH). This study is approved by Institutional Review Board (IRB) at Rutgers, The State University of New Jersey (IRB application # Pro2018002356). Patients were selected for whom a clinical test was ordered by a physician, and we were provided de-identified left-over blood samples which didn't require the informed consent in accordance with the IRB guidelines. Blood sample acquisition and all the experiments were done according with the IRB protocol guidelines.

2.6 Neutrophil isolation and functionalization

For isolating neutrophils from whole blood, deidentified patient blood samples were collected from RWJMH. Following collection from patients, blood was processed to isolate human neutrophils, with their corresponding lactate levels recorded. Blood was then combined with equal parts 1X PBS, and 1.8 mL was mixed with 2.4 mL of Ficoll-Paque density gradient. The solution was centrifuged for 30 minutes at 400g to separate plasma, platelets, and red blood cells, followed by supernatant aspiration and addition of 3 mL of deionized (DI) water for 15 secs to lyse non-neutrophil mononuclear cells. After 15 secs, 0.3 mL of 10X PBS was added for tonicity restoration, and the solution was further centrifuged for 5 minutes at 300g. The previous step was repeated until a neutrophil pellet formed, which was resuspended in RPMI 1640 with 50 μL of cells to 5 mL of media[49].

Once prepared, a 200 μL solution of either 10 nm Al_2O_3 coated-Janus microparticles with functionalized anti-CD11b antibody (10nmMOJPs/anti-CD11b) or 30 nm Al_2O_3 coated-Janus microparticles with functionalized anti-CD66b antibody (30nmMOJPs/anti-CD66b) at $5.92x10^7$ particles/mL each were mixed with 1 mL of cells diluted in 1X PBS followed by 1-hour incubation. For samples without MOJPs added (cells alone), the isolated neutrophils were diluted in 1X PBS and incubated for 1 hour.

For flow cytometry of the same sample, 20 μL of aliquoted either FITC-CD66b or PE-CD11b test solution was added to 100 μL of diluted neutrophils in 1X PBS (~$1.0x10^5$ cells/mL) and incubated in the dark prior to analysis, per the manufacturers' protocol. The "Open Flow Cytometry" setting was selected on the Moxi Go II, the FITC and PE filters were installed, and 60 μL of sample was pipetted into the loading cartridge after device calibration.

2.7 Signal acquisition, demodulation, and data processing

The middle electrode was voltage stimulated with 500 kHz, 1 MHz, 2 MHz, and 3 MHz input frequencies, while exterior electrodes were grounded (Fig. 1a-c) in series with 10kΩ resistors. The signal acquisition process flow is outlined in Fig. 1c and in greater detail with ESI Fig. 1a. LabView custom script was developed for signal acquisition. First, the device's current recordings were converted to voltage and increased through transimpedance amplification. After, the two input signals fed to a differential amplifier, and subsequent sampled at 250 kHz. Following signal acquisition, a lock-in amplifier demodulated and isolated the four frequencies into distinct arrays (Fig. 1c). Digital filters were then applied using MATLAB and detailed in ESI Fig. 1b to normalize signal and reduce background noise. Here, a 4^{th} order Butterworth filter high pass filter removes data below 20 Hz to remove any drifts in baseline voltage values. A 4^{th} order Butterworth filter low pass filter removes data above 100 kHz, and 1^{st} order Butterworth band-stop filters remove powerline interference at 60 Hz and 120 Hz. Digital filtering is achieved via the MATLAB Signal Processing Toolbox, and raw electrical recordings are simultaneously produced over time in the electrical recording regime for each input frequency (Fig. 1d). A voltage threshold of 5 times the noise standard deviation determines neutrophil or neutrophil-particle conjugate presence, and the difference between the maximum and minimum voltage values recorded within 500 data points of the pulse threshold triggering determines the pulse bipolar amplitude. Positive pulse, negative pulse, and peak-to-peak pulse amplitudes were recorded for each object across the four demodulated voltage frequencies under impedance cytometry.

2.8 Fluorescence microscopy protocol

Biotin-4-fluorescein (B4F) and Atto 655-biotin (BA655) were each dissolved in separate solutions of dimethyl sulfoxide (DMSO) to form a 0.08 mg/mL concentration. After SAv addition to the microparticle solution, incubation and washing steps were performed prior to adding antibodies. Subsequently, 10 μL of B4F in DMSO (0.08 mg/mL) was added to a 200 μL sample of 30 nm MOJPs with adsorbed SAv. In parallel, 10 μL of BA655 in DMSO was added to a 200 μL sample of 10 nm MOJPs after SAv adsorption. This was followed by 10 seconds of vortexing and 5 minutes of ultrasonic agitation to thoroughly mix the

biotinylated dyes with the SAv-adsorbed microparticles, as DMSO and 1X PBS combines. After mixing, the sample was incubated for 1 hour to ensure strong SAv-biotin binding before fluorescence analysis.

ImageJ was used for image processing and fluorescent quantification. Particle pixel intensity was compared to background pixel intensity using an aligned line segment connecting particles across the image space and pixel values were recorded. For measuring maximum pixel intensity from particles, rectangular segments were plotted over particle regions and maximum pixel values were recorded. False coloring was performed by converting the image to an RGB color image, then the image was composited, with split channels between green and red intensities.

3 Results and discussion

3.1 Anti-CD11b and anti-CD66b fluorescence microscopy with unique MOJPs

Both 10nm MOJPs with absorbed SAv and bound BA55 and 30 nm MOJPs with adsorbed SAv and bound B4F were imaged under brightfield and fluorescence microscopy. False coloring was used in ImageJ to better differentiate particles under fluorescence. From Fig. 2, both B4F (Fig. 2a and 2d) and BA655 (Fig. 2b and 2e) were observed directly over MOJP positions in the image and absent in regions without particles. This confirms SAv absorption on both particle surfaces and purification steps removes unbound SAv from the solutions. When both solutions were combined and imaged (Fig. 2c and 2f), the results show the functionalized particles retain their corresponding dye and do not lose binding. Here, it signifies the capacity for these MOJPs to be patterned with different targeting antibodies and be used in the same solution without losing functionalization or biotinylated antibodies off-binding to unintended MOJPs.

3.2 Observing correlated amplitude regression for neutrophil samples with different MOJPs

From the same patient blood sample, isolated neutrophils underwent flow cytometry staining (ESI† Fig. 2) and impedance cytometry both targeting CD11b and CD66b receptors. Impedance cytometry data was collected in independent samples for cells without MOJPs particles (Neutrophils alone, Fig. 3ai, 3bi, 3ci), cells with possibly conjugated 10nmMOJPs/CD11b particles (Neutrophils/10nmMOJPs/anti-CD11b, Fig. 3aii, 3bii, 3cii), and cells with possibly conjugated 30nmMOJPs/CD66b (Neutrophils/30nmMOJPs/anti-CD66b, Fig. 3aiii, 3biii, 3ciii).

Fig. 3 analyzes the recorded bipolar amplitudes across the different sample conditions as scatter plots comparing two different frequencies. When measured in reference to the 500 kHz voltage frequency, it is observed that bipolar amplitude decreases for each sample type with increasing voltage frequency due to neutrophil membrane conductance[50]. Since MOJPs are frequency-dependent based on their shell conductance as well, it is expected that cells with conjugated MOJPs will have relatively lower amplitudes at higher frequencies dependent on the thickness of its aluminum oxide coating[46]. Fig. 3 and Fig. 4 reveal slight changes in the slope of these bulk samples when measuring their average linear regression trendline (additional Fig. 4 data presented in ESI Fig. 3). Originally, comparing the trendline slope of 1 MHz versus 500 kHz, the Neutrophils alone group has the lowest slope, with Neutrophils/10nmMOJPs/anti-CD11b having a higher slope and Neutrophils/10nmMOJPs/anti-CD11b having the highest slope between groups (Fig. 3a). This trend changes however with increasing voltage frequency, as the Neutrophils/10nmMOJPs /anti-CD11b group shifts to having the lowest slope of the 2 MHz versus 500 kHz average trendline group (Fig. 3b). This indicates the participation in impedance reduction of the 10nm MOJPs from these particles based on their conjugation to CD11b receptors on neutrophils.

The greatest separation between linear regression slopes when observing two different frequencies occurred between the bipolar amplitudes of 3 MHz versus 1 MHz (Fig. 4 and ESI Fig. 3), which saw the largest disparity between Neutrophils alone and Neutrophils/10nmMOJPs/anti-CD11b with a 22% reduction. For the Neutrophils/30nmMOJPs/anti-CD66b groups, comparisons with higher frequencies to a 1 MHz reference frequency (ESI Fig. 3) reduced the slope value compared to the control neutrophils without incubated particles. This is where the hypothesized impedance shift is expected to occur for 30nm MOJPs and its involvement in a lower linear slope at these frequencies results from these particles binding to CD66b receptors on neutrophils.

Unlike the flow cytometry staining of CD66b and CD11b (ESI Fig. 2 and Table 1), analyzing bivariate changes in bipolar amplitude are unable to quantify the number of neutrophils which have particles attached as the changes in the individual pulses in the groups are too insignificant to develop characteristic pulses. While neutrophils were incubated with functionalized MOJPs, it would not be expected that all neutrophils in the sample would undergo particle conjugation. Most likely it would translate similarly to the proportion of cells identified with receptor expression from flow cytometry, although the binding of MOJPs to neutrophils depending on the degree of their corresponding receptor expression or the number of MOJPs bound to one cell has not yet been evaluated. For the results so far, only the bulk changes in these samples have been observed. Additional multivariate studies must be conducted to further refine the differences between the data points in each sample to determine if individual pulses can be confirmed as neutrophil-particle conjugates, and if these conjugates correspond to the percentage of cells that were measured with higher expression values in the flow cytometry results.

3.3 Differentiation accuracy after classified machine learning of bulk sample data

After observing bivariate frequency-dependent bipolar amplitude changes between neutrophil samples which did or did not contain receptor functionalized MOJPs and not determining significant differences, machine learning was

applied to assess individual characteristic changes across their recorded data spectrum. Here, the 'Classification Learner' application in MATLAB facilitated training and testing of various machine learning models from neural networks, support vector machines, Naïve Bayes, ensemble classifiers, and more, using the same data sets from the previous section. The pulses data for each cohort was randomized, and of the over 5000 pulses recorded for each group, 3500 pulses were used for model training and 1500 were used for testing. For each pulse recorded, the machine learning models are measuring changes across bipolar amplitude, the positive amplitude peak, and the negative amplitude peak for the four frequencies, totaling 12 interlaced features.

Table 1 summarizes the machine learning results which the greatest testing accuracy when comparing two samples across their feature data and the ability to correctly determine the individual pulses. All comparisons show greater than 79% accuracy in differentiating the pulse data from the two groups, as well as area under the receiver operating curves (ROC AUC) above 85% and high sensitivities and specificities (Fig. 5). This also includes the ability to accurately differentiate the MOJPs included groups from each other, which will be critical to measure these receptors in a combined multiplexed sample. For the three different comparisons, a narrow neural network recorded the highest testing accuracy. This model used a single connected layer with 10 nodes and a rectifier activation function.

A greater picture is revealed in the ability to discern electrical characteristics between the samples, as these differences may be directly due to pulse data from cells having conjugated MOJPs attached exhibiting unique pulse amplitudes across the different frequencies. This improved accuracy compared to only measuring the bulk change in the bivariate linear regression slope may be due to the nature of the MOJP's frequency-dependent impedance shift being more identifiable across multiple frequencies rather than observing changes in two frequencies alone. With machine learning, this higher dimensional analysis is performed and has greater ability to observe these behaviors. It was also expected that expression resulting from conjugation of 30nm MOJPs would yield greater signal contrast to cells alone compared to the signal difference for 10nm MOJPs as the thicker coating has a greater shell conductance and would have a larger amplitude reduction at higher frequencies[46]. This may justify why the Cells alone compared to the Cells/30nmMOJP/anti-CD66b group recorded the highest accuracy and highest area under the curve, although this trend was not previously determined in the previous section (Fig. 5b). However, with this machine learning dissemination there is still an inability to identify conjugation at a single pulse level for the mixed samples (Cells/30nmMOJP /anti-CD66b and Cells/10nmMOJP/anti-CD11b). Indeed, these machine learning results are still only measuring pulse differences from observing trends of the bulk samples, and presently the number of cells with expressed receptors is not known. The accuracies determined may infer greater conjugation, as the Cells/30nmMOJP/anti-CD66b may not have the highest differentiation accuracy compared to Cells Alone due to greater shell conductance as discussed previously but may be due to a greater number of cells had 30nm MOJPs conjugated and therefore the frequency-dependent impedance shift was more significant to the bulk sample. It was observed still that there are significant differences related to the sample pulse amplitudes correlated to the presence of MOJPs.

3.4 Identifying conjugate groups using unsupervised clustering

One option to declassify high order groups within the samples is to employ unsupervised machine learning, since the individual pulses are not referenced to conjugation. Here, it is proposed that the largest contributor to pulse amplitude changes between samples are the result of conjugated MOJPs, and that these shifts would be present in mixed samples. If two clustered groups are selected for unsupervised machine learning, it is expected that one population would represent neutrophil-MOJP conjugates and the other would represent cells without conjugated MOJPs.

Using MATLAB, clustering was performed after log normalizing each pulse feature across the different frequencies, with a hierarchy of grouping performed. For these cases, the positive amplitude (PA) and negative amplitude (NA) variability was measured for each frequency, with the rationale that greater pulse resolution can be measured as opposed to the bipolar pulse alone. A heat map was generated displaying the variance within feature groups and how the collective pulse characteristics for individual data points generated binned separation (Fig. 6). Here, darker hue indicates a logarithmically normalized data value is farther away from the feature group's mean, with darker red color greater in magnitude than the feature average and dark blue color less than the feature average. The data points are arranged in such a way to group as many similar feature variations per data point as possible, represented by the top hierarchical axis. For the "Neutrophils alone" sample (Fig. 6a), the highest grouping class rendered two equal distributions, which is interpreted as low variability in the bulk sample and acts as a control when observing clustering trends for the MOJPs mixed samples. Interestingly, different group proportions are noticed with these mixed samples (Fig. 6b and c), with skewed group sizes and greater internal feature variance. When studying the highest order clustering, the two most distinct groups are separated by the red line in the heat map, and the different groups are assigned either "group 1" as the smaller grouping and "group 2" as the larger. This dichotomy in groupings from the Neutrophils alone and the mixed samples further points towards the influence of possible MOJP conjugation, and these distributions may allow quantification of cells with MOJP attachment.

After clustering and observing group behavior differences for the mixed samples, the separated pulse data is extracted and recorded for supervised machine learning similar to the previous section. For each group, approximately 75% of the randomized data points were used for machine learning training and 25% were used for testing. Now, it is expected one of the groups have greater differentiation accuracy compared to the Neutrophils alone sample, and it is hypothesized that this

group contains only neutrophil-MOJP data. Table 2 and Fig. 7 summarizes these relationships, where the separated clusters labeled as "group 1" for both the Cells/10nmMOJP/anti-CD11b sample and Cells/30nmMOJP/anti-CD66b recorded higher differentiation accuracies and ROC AUC compared to their divided group 2s. For these cases, all of them reported the highest testing accuracies with the narrow neural network model, which both group 1s attaining greater than 91% differentiation accuracy to the Cells alone sample. Again, group 1 for Cells/10nmMOJP/anti-CD11b represented 28.9% of the entire sample, while group 1 for Cells/30nmMOJP/anti-CD66b corresponded to 35.9% of the bulk sample.

While compared to the flow cytometry results for the same neutrophil distribution (ESI Fig. 2), these percentages align with the receptor expression for CD66b, but under reports for CD11b expression. This may be due to MOJPs conjugating to cells requiring a different expression threshold to occur versus flow cytometry expression, which would result in different counts for cells with targeted expression. Additionally, while these studies have separated out the highest order group between mixed samples, it still may not directly translate to cell-particle conjugate data, as the individual pulse identities are still unknown. At this current juncture, these results can only point towards a relationship with pulse amplitude and cell-MOJPs conjugates, and since this technology and its methodology is novel, future characterizations must be conceived to better control pulse data.

As the following preliminary results are promising for directing this technology for receptor expression quantification, there are still many forthcoming experiments to characterize the different MOJP signals when conjugated to cells and hypothesizing valid control tests. Currently, flow cytometry is being used to generate expression of bulk sample data, but this is not robust enough at this stage for confirming impedance cytometry differences are entirely due to cell-particle conjugation. One future test planned is to stain the functionalized MOJPs with biotinylated dyes to obtain both conjugation and fluorescence potential at the same time. After incubation with cells, the sample will be analyzed using the Moxi GO II flow cytometer which has both fluorescence and particle size functionality. From this, mean fluorescence intensity recordings for objects larger than the size of neutrophils may confirm particle-cell conjugation, and fluorescence would only occur around the particles. Additional strategies may include using a high-speed camera with a microscope to obtain video recordings for particles traveling over the electric field in the microfluidic impedance cytometry. Using a slower flow rate and more diluted samples, individual cell or cell-particle conjugates may be video recorded and overlayed with pulse data to have more individual control in impedance pulse identity.

4 Conclusion

In this article, the use of voltage frequency-sensitive aluminum oxide-coated microparticles were explored to quantify neutrophil expression of CD11b and CD66b receptors using functionalized antibody targeting. When observing bipolar amplitude trends at different input frequencies from recorded impedance cytometry counts, there were shifts in bulk linear slopes across two frequencies depending on the MOJP coating thickness included with the sample. Supervised machine learning was then used to greater disseminate different samples and recorded accuracies above 75%, but the quantity of cells with conjugated MOJPs within mixed samples was still unknown. Next, unsupervised machine learning was employed to determine groups within samples which may correspond to separating cell-particle conjugates from unconjugated particles. Finally, these groups were extracted and supervised machine learning revealed accuracies above 91% when comparing groups suspected as solely neutrophil-MOJP data compared to neutrophil samples without mixed particles. However, refined pulse identities are still unknown across experiments, and future characterization studies are proposed to directly tag individual pulses to indicate cell-particle conjugation or not, included high-speed video microscopy to record their state in real time. These future studies are currently underway to optimize conditions for simultaneous impedance and high-speed video microscopy recordings.

Should these future characterization tests prove successful, a later goal is to refine characteristic pulse signatures representing attached MOJPs and their corresponding identity in a mixed heterogenous samples. Here, both 10nmMOJP/anti-CD11b particles and 30nmMOJP/anti-CD66b particles would be incubated with isolated neutrophils in one sample to distinguish the different cell-particle conjugate conditions, with one, both, or neither particle types conjugated to cells when measured under multifrequency impedance cytometry being identified. Once achieved, unknown samples can be measured, and greater accuracy can be used to both obtain information into which cells are expressing what receptors and the percentage of sample expression. Since these particles have proven to be electrically determined in previous studies[46], more than two MOJPs may be used in a sample for receptor targeting after these signatures are determined from a specific device design. Different cells and different cell receptors may be measured in the same sample, including nCD64, mHLA-DR, TLR, CD28, and more, and greater sensitivity may be realized with this multiplexed approach. With a streamlined sample processing approach, such a system can analyze biomarkers faster, with more automation, and with higher multiplexing potential than current gold standard techniques like flow cytometry, which may improve disease diagnostics in critical care settings.

Author Contributions

B.K.A. participated in: Methodology, Data curation, Formal analysis, Funding acquisition, Visualization, Writing – original draft, Writing – review & editing. J.S. participated in: Methodology. M.D. participated in: Conceptualization, Supervision, Writing – review & editing. U.H. participated in: Conceptualization, Funding acquisition, Supervision, Writing – review & editing.

Conflicts of interest

U.H. is a cofounder and owns small equity in a start-up company (Prenosis Inc). Rest of authors declare no conflict of interest.

Acknowledgements

Authors would like to acknowledge the funding support from the Rutgers, The State University of New Jersey School of Engineering. Authors also acknowledge support from the National Science Foundation (NSF) Award Number 2002511 and the National Institute of General Medical Sciences (NIGMS) as part of the National Institute of Health's (NIH) training grant T32 GM135141.

References

1 D. Saygin, N. Wanner, J. A. Rose, S. V. Naga Prasad, W. H. W. Tang, S. Erzurum and K. Asosingh, *Cytometry Part A*, 2018, **93**, 563–570.
2 H. Jin, M. Aziz, Y. Ode and P. Wang, *Shock*, 2019, **51**, 548–556.
3 E. S. Graham, C. E. Angel, L. E. Schwarcz, P. R. Dunbar and M. Glass, *Int J Immunopathol Pharmacol*, 2010, **23**, 25–34.
4 L. M. Park, J. Lannigan and M. C. Jaimes, *Cytometry Part A*, 2020, **97**, 1044–1051.
5 T. Maetzig, J. Ruschmann, C. K. Lai, M. Ngom, S. Imren, P. Rosten, G. L. Norddahl, N. von Krosigk, L. Sanchez Milde, C. May, A. Selich, M. Rothe, I. Dhillon, A. Schambach and R. K. Humphries, *Molecular Therapy*, 2017, **25**, 606–620.
6 V. N. Umlauf, S. Dreschers and T. W. Orlikowsky, *International Journal of Pediatrics*, 2013, **2013**, 763191.
7 B. K. Ashley and U. Hassan, *WIREs Nanomedicine and Nanobiotechnology*, 2021, **13**, e1701.
8 L. Boneschansker, J. Yan, E. Wong, D. M. Briscoe and D. Irimia, *Nature Communications*, 2014, **5**, 4787.
9 F. Ellett, J. Jorgensen, A. L. Marand, Y. M. Liu, M. M. Martinez, V. Sein, K. L. Butler, J. Lee and D. Irimia, *Nature Biomedical Engineering*, 2018, **2**, 207–214.
10 L. L. Sun, Y. S. Leo, X. Zhou, W. Ng, T. I. Wong and J. Deng, *Materials Science for Energy Technologies*, 2020, **3**, 274–281.
11 K. Cihalova, D. Hegerova, A. M. Jimenez, V. Milosavljevic, J. Kudr, S. Skalickova, D. Hynek, P. Kopel, M. Vaculovicova and V. Adam, *Journal of Pharmaceutical and Biomedical Analysis*, 2017, **134**, 325–332.
12 V. Herrera, S.-C. Joseph Hsu, M. K. Rahim, C. Chen, L. Nguyen, W. F. Liu and J. B. Haun, *Analyst*, 2019, **144**, 980–989.
13 O. A. Saleh and L. L. Sohn, *Proc Natl Acad Sci U S A*, 2003, **100**, 820–824.
14 J. Sui, N. Gandotra, P. Xie, Z. Lin, C. Scharfe and M. Javanmard, *Sci Rep*, 2021, **11**, 6490.
15 S. Gawad, L. Schild and P. Renaud, *Lab on a Chip*, 2001, **1**, 76–82.
16 J. Zhong, M. Liang and Y. Ai, *Lab on a Chip*, 2021, **21**, 2869–2880.
17 Th. Schnelle, T. Müller and G. Fuhr, *Journal of Electrostatics*, 2000, **50**, 17–29.
18 B. K. Ashley and U. Hassan, *Biotechnology and Bioengineering*, 2021, **118**, 4428–4440.
19 M. Carminati, L. Pedalà, E. Bianchi, F. Nason, G. Dubini, L. Cortelezzi, G. Ferrari and M. Sampietro, *Sensors and Actuators A: Physical*, 2014, **219**, 80–87.
20 P. Ciccarella, M. Carminati, M. Sampietro and G. Ferrari, in *2016 IEEE International Solid-State Circuits Conference (ISSCC)*, 2016, pp. 486–488.
21 A. U. Alam, D. Clyne, H. Jin, N.-X. Hu and M. J. Deen, *ACS Sens.*, 2020, **5**, 412–422.
22 B. C. Colson and A. P. M. Michel, *ACS Sens.*, 2021, **6**, 238–244.
23 K. Reinosdotter and M. Viklander, *Water Quality Research Journal*, 2007, **42**, 153–161.
24 A. Baraket, M. Lee, N. Zine, M. Sigaud, J. Bausells and A. Errachid, *Biosensors and Bioelectronics*, 2017, **93**, 170–175.
25 U. Hassan, T. Ghonge, B. R. Jr, M. Patel, M. Rappleye, I. Taneja, A. Tanna, R. Healey, N. Manusry, Z. Price, T. Jensen, J. Berger, A. Hasnain, E. Flaugher, S. Liu, B. Davis, J. Kumar, K. White and R. Bashir, *Nature Communications*, 2017, **8**, 15949.
26 D. C. Spencer, T. F. Paton, K. T. Mulroney, T. J. J. Inglis, J. M. Sutton and H. Morgan, *Nat Commun*, 2020, **11**, 5328.
27 S. Zhang, Z. Han, Z. Feng, M. Sun and X. Duan, in *2021 43rd Annual International Conference of the IEEE Engineering in Medicine Biology Society (EMBC)*, 2021, pp. 7087–7090.
28 N. Talukder, A. Furniturewalla, T. Le, M. Chan, S. Hirday, X. Cao, P. Xie, Z. Lin, A. Gholizadeh, S. Orbine and M. Javanmard, *Biomed Microdevices*, 2017, **19**, 36.
29 U. Hassan, B. Reddy, G. Damhorst, O. Sonoiki, T. Ghonge and C. Yang, *TECHNOLOGY*, 2015, **03**, 1550009.
30 S. Dellepiane, M. Marengo and V. Cantaluppi, *Crit Care*, 2016, **20**, 61.
31 K. M. Irvine, L. F. Wockner, I. Hoffmann, L. U. Horsfall, K. J. Fagan, V. Bijin, B. Lee, A. D. Clouston, G. Lampe, J. E. Connolly and E. E. Powell, *PLOS ONE*, 2016, **11**, e0167001.
32 T. Liu, M. L. Y. Sin, J. D. Pyne, V. Gau, J. C. Liao and P. K. Wong, *Nanomedicine: Nanotechnology, Biology and Medicine*, 2014, **10**, 159–166.
33 M. Adib, V. Ostadi, F. Navaei, F. S. Fosoul, F. Oreizi, R. Shokouhi and Z. Bakhshiani, *Iranian Journal of Allergy, Asthma and Immunology*, 2007, 93–96.
34 I. Nupponen, S. Andersson, A.-L. Järvenpää, H. Kautiainen and H. Repo, *Pediatrics*, 2001, **108**, e12.
35 J. Jämsä, V. Huotari, E. Savolainen, H. Syrjälä and T. Ala-Kokko, *Critical Care*, 2012, **16**, P41.
36 T. Schmidt, J. Zündorf, T. Grüger, K. Brandenburg, A.-L. Reiners, J. Zinserling and N. Schnitzler, *Journal of Leukocyte Biology*, 2012, **91**, 791–802.
37 A. Sheneef, T. Mohamed, N. F. Boraey and M. Ashry, *Egypt J Immunol*, 2017, **24**, 29–36.
38 R. V. Sionov, Z. G. Fridlender and Z. Granot, *Cancer Microenvironment*, 2015, **8**, 125–158.
39 M. Ilie, V. Hofman, C. Ortholan, C. Bonnetaud, C. Coëlle, J. Mouroux and P. Hofman, *Cancer*, 2012, **118**, 1726–1737.
40 H. K. Jensen, F. Donskov, N. Marcussen, M. Nordsmark, F. Lundbeck and H. von der Maase, *JCO*, 2009, **27**, 4709–4717.
41 F. Boissière-Michot, W. Jacot, J. Fraisse, S. Gourgou, C. Timaxian and G. Lazennec, *Cancers*, 2020, **12**, 2076.
42 S. Q. Khan, I. Khan and V. Gupta, *Front. Med.*, , DOI:10.3389/fmed.2018.00052.
43 V. A. Manivel, A. Sohrabian, M. C. Wick, M. Mullazehi, L. D. Håkansson and J. Rönnelid, *Arthritis Research & Therapy*, 2015, **17**, 8.
44 Torsteinsdóttir, Arvidson, Hällgren, and Håkansson, *Scandinavian Journal of Immunology*, 1999, **50**, 433–439.
45 P. Xie, X. Cao, Z. Lin and M. Javanmard, *Lab on a Chip*, 2017, **17**, 1939–1947.
46 J. Sui, P. Xie, Z. Lin and M. Javanmard, *Talanta*, 2020, **215**, 120791.
47 T. Calais, D. Bourrier, A. Bancaud, Y. Chabal, A. Estève and C. Rossi, *Langmuir*, 2017, **33**, 12193–12203.
48 B. K. Ashley, J. Sui, M. Javanmard and U. Hassan, *Anal Bioanal Chem*, 2021, **413**, 555–564.
49 K. Wagner, M. A. Sami, C. Norton, J. McCoy and U. Hassan, *RSC Advances*, 2021, **11**, 21315–21322.
50 T.-X. Zhao, B. Jacobson and T. Ribbe, *Physiol. Meas.*, 1993, **14**, 145–156.

Table 1: Differentiating complete sample data using machine learning

Machine Learning Sample Differentiation	Accuracy	ROC AUC	Sensitivity	Specificity
Cells alone vs. Cells/10nmMOJP/anti-CD11b	75.8%	85.0%	69.0%	82.5%
Cells alone vs. Cells/30nmMOJP/anti-CD66b	82.8%	92.0%	81.6%	84.0%
Cells/10nmMOJP/anti-CD11b vs. Cells/30nmMOJP/anti-CD66b	79.5%	87.0%	84.8%	74.2%

Table 2: Differentiating sample data using machine learning after unsupervised sample grouping

Machine Learning Sample Differentiation	Accuracy	ROC AUC	Sensitivity	Specificity	% Group data points
Cells alone vs. Cells/10nmMOJP/anti-CD11b Group 1	91.7%	97.0%	82.0%	94.1%	28.9%
Cells alone vs. Cells/10nmMOJP/anti-CD11b Group 2	75.5%	84.0%	63.4%	82.8%	71.1%
Cells alone vs. Cells/30nmMOJP/anti-CD66b Group 1	91.3%	96.0%	78.4%	95.1%	35.9%
Cells alone vs. Cells/30nmMOJP/anti-CD66b Group 2	85.7%	93.0%	77.3%	90.2%	64.1%

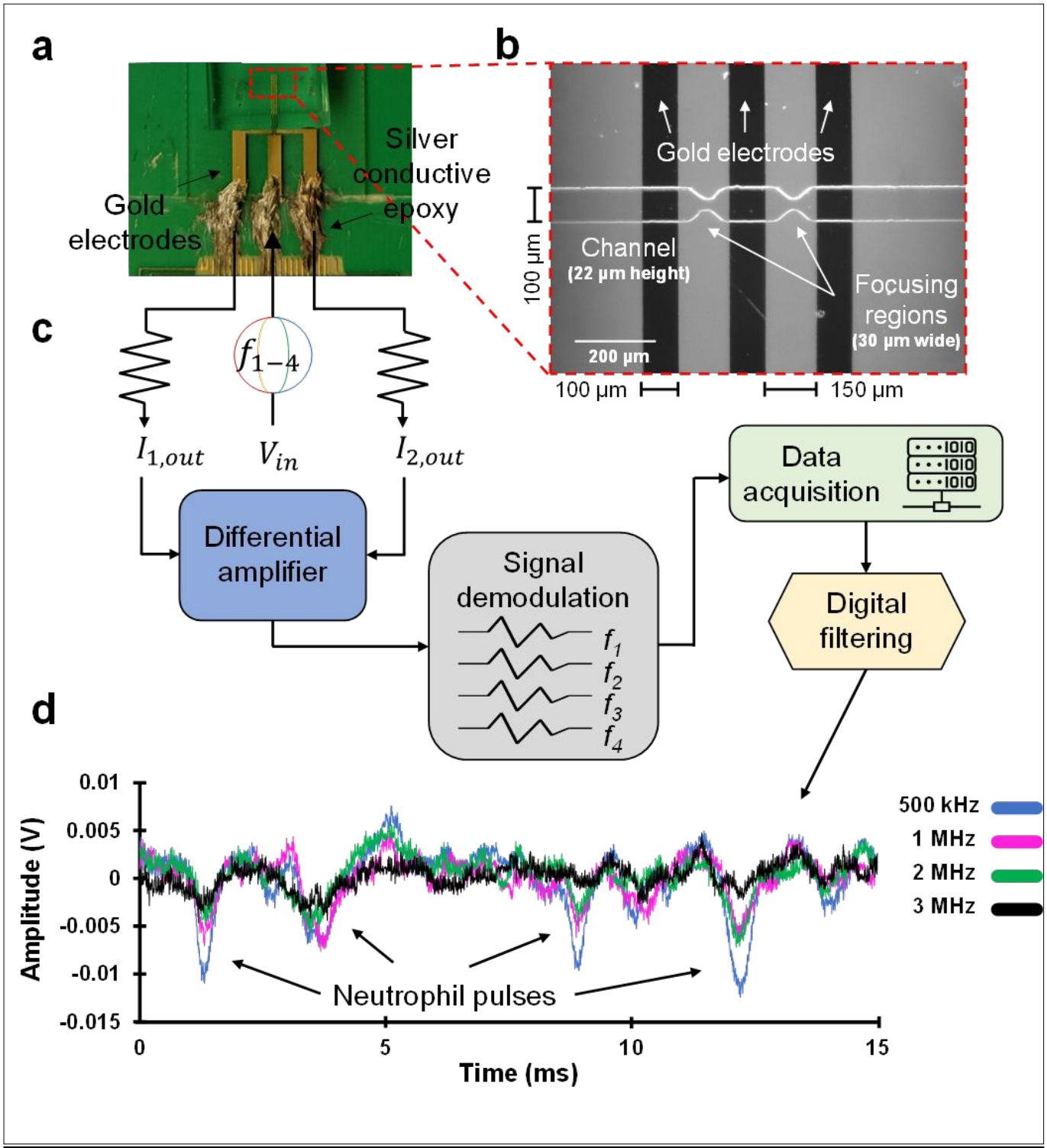

Fig. 1 Overview of multifrequency impedance cytometry device and microparticle detection scheme. a) Image of device with microfabricated gold electrodes supporting PDMS-based microfluidic channels. Gold electrodes are connected to a custom printed circuit board with silver conductive epoxy to interface a multifrequency voltage input and grounded electrode recordings through a lock-in amplifier. b) Microscope image of microfluidic channel with focusing regions positioned between coplanar electrodes, increasing detection sensitivity. c) Flow chart of data collection, signal demodulation from four input voltage frequencies, and signal processing to produce voltage data. d) Representative time-domain results of voltage data, with four demodulated frequencies aligned to show pulses from isolated neutrophils flowing through the channel.

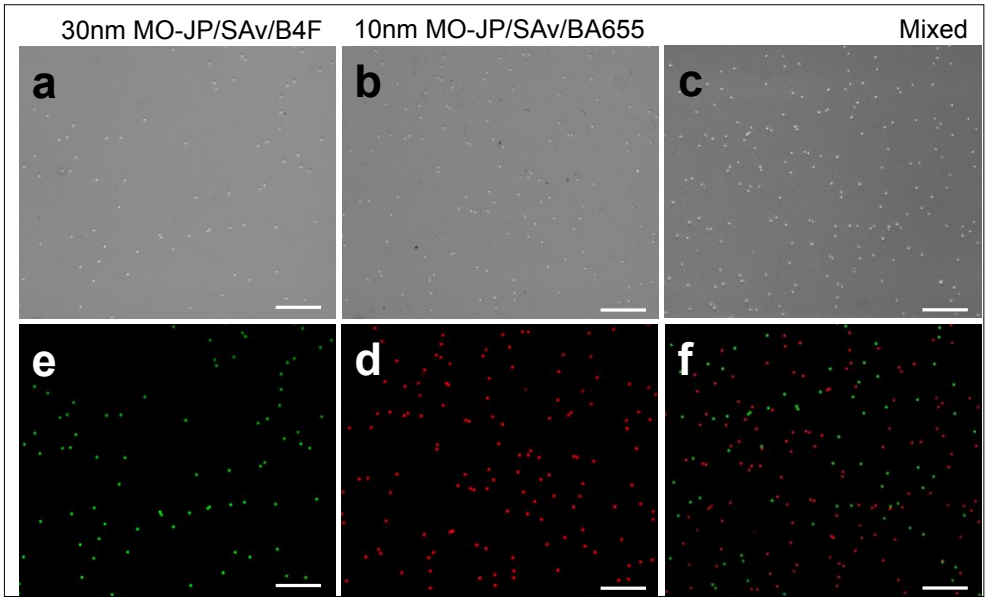

Fig. 2 Brightfield (a-c) and false-colored fluorescence (d-f) imaging of 30 nm aluminum oxide-coated Janus microparticles (MOJP) functionalized with biotin-4-fluorescein dye (green) after streptavidin (SAv) adsorption and 10 nm MOJPs functionalized with biotinylated-Atto 655 (red) after SAv adsorption. False coloring performed with ImageJ, scale bars = 40 µm.

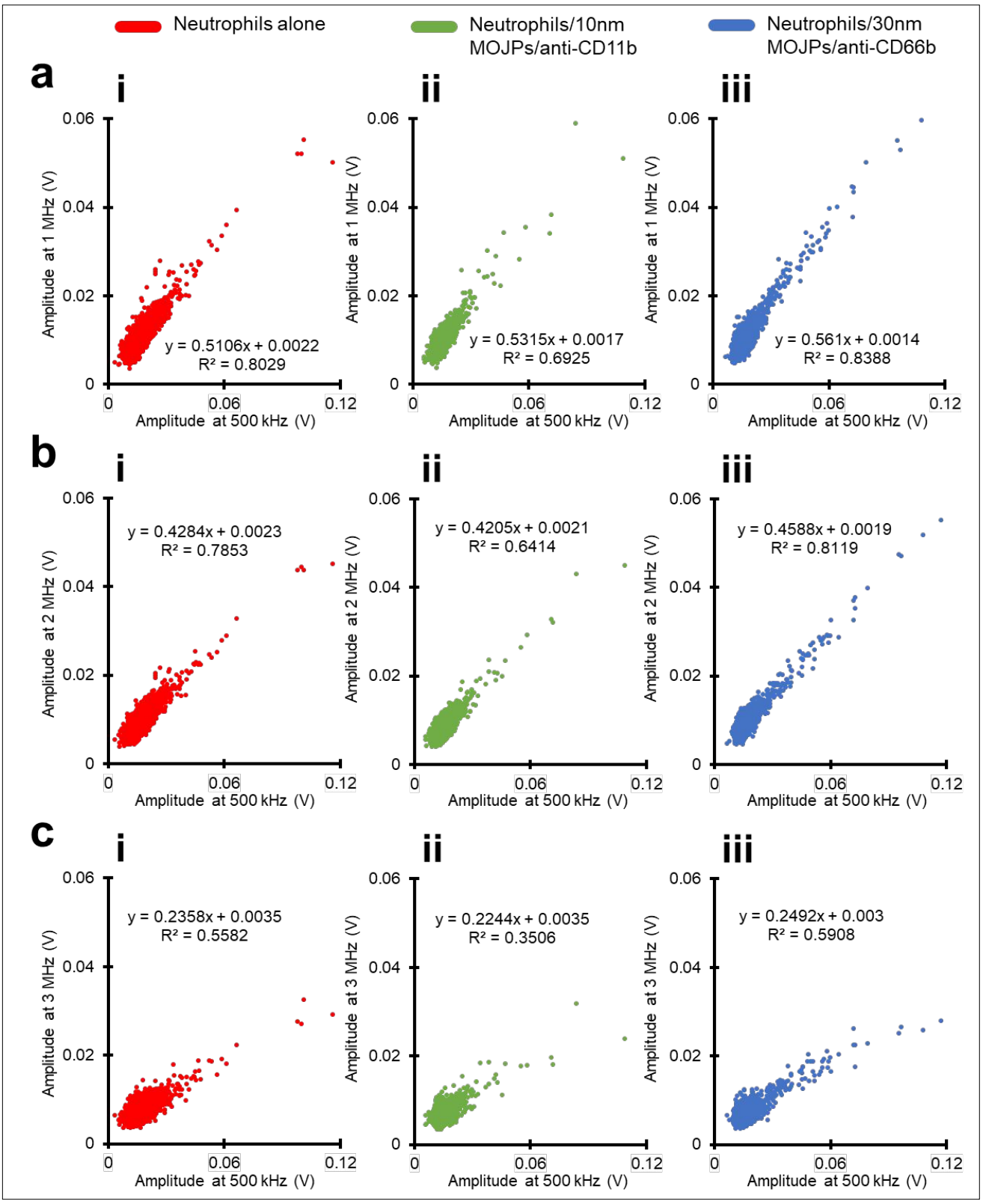

Fig. 3 Scatter plots of bipolar amplitude data collected from multifrequency impedance cytometry. Red: isolated neutrophils alone (i), green: neutrophils combined with 10 nm aluminum oxide coated Janus microparticles (MOJPs) functionalized with anti-CD11b antibodies (ii), blue: neutrophils combined with 30 nm MOJPs functionalized with anti-CD66b antibodies (iii). Bivariate data displaced across the higher frequencies compared to lower 500 kHz reference frequency. a) 1 MHz, b) 2 MHz, and c) 3 MHz.

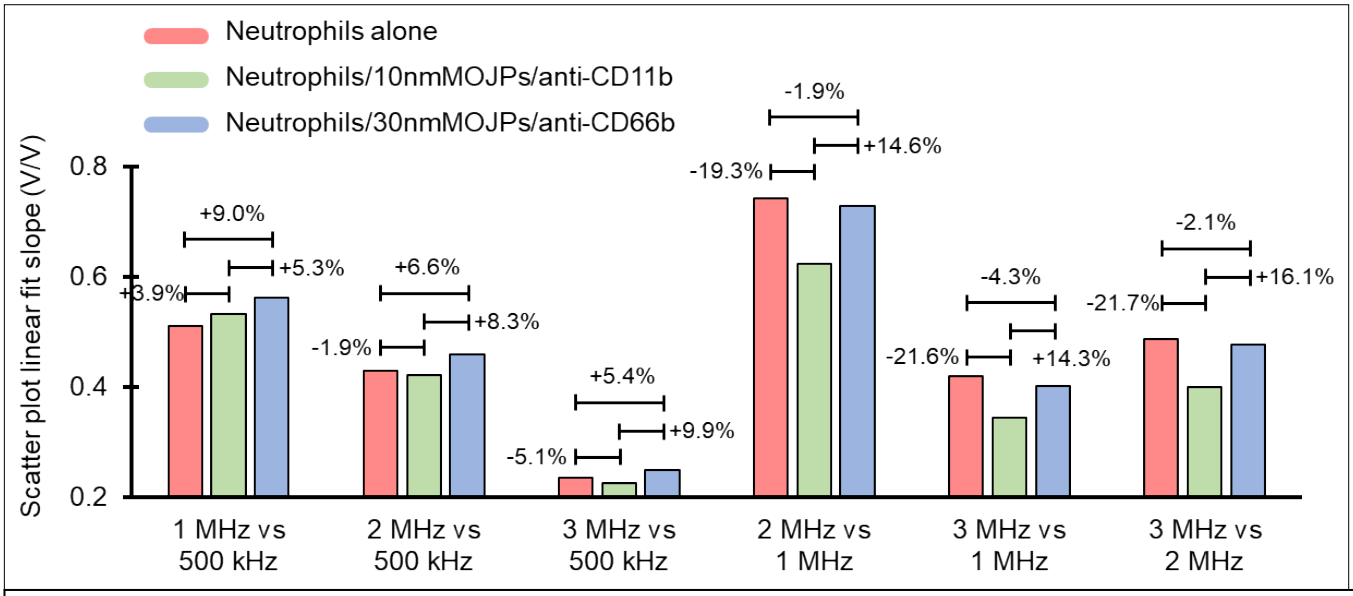

Fig. 4 Bar plots comparing line of best fit slopes from impedance cytometry pulse data across different frequencies, referenced in Fig. 3 and ESI Fig. 2 (red: isolated neutrophils alone, green: neutrophils combined with 10 nm aluminum oxide coated Janus microparticles (MOJPs) functionalized with anti-CD11b antibodies, blue: neutrophils combined with 30 nm MOJPs functionalized with anti-CD66b antibodies). Percentages are percent change in linear regression slopes in reference to the leftmost species. Nomenclature shown as "y-axis frequency vs x-axis frequency".

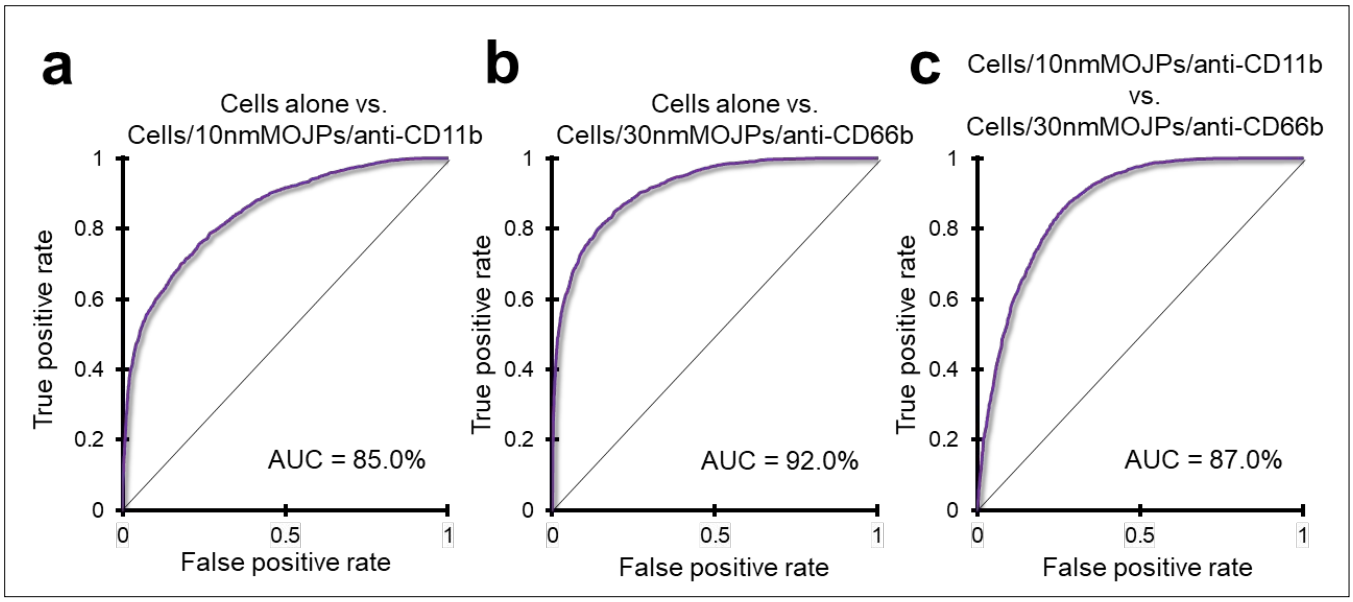

Fig. 5 Receiver operating curves classifying all multifrequency impedance cytometry pulse data. a) Comparing isolated neutrophils (Cells Alone) to neutrophils combined with 10 nm aluminum oxide coated Janus microparticles (MOJPs) functionalized with anti-CD11b antibodies (Cells/10nmMOJP/anti-CD11b). b) Cells Alone versus neutrophils combined with 30 nm MOJPs functionalized with anti-CD66b antibodies (Cells/30nmMOJP/anti-CD66b). c) Cells/10nmMOJP/anti-CD11b vs. Cells/10nmMOJP/anti-CD11b. AUC = area under the curve.

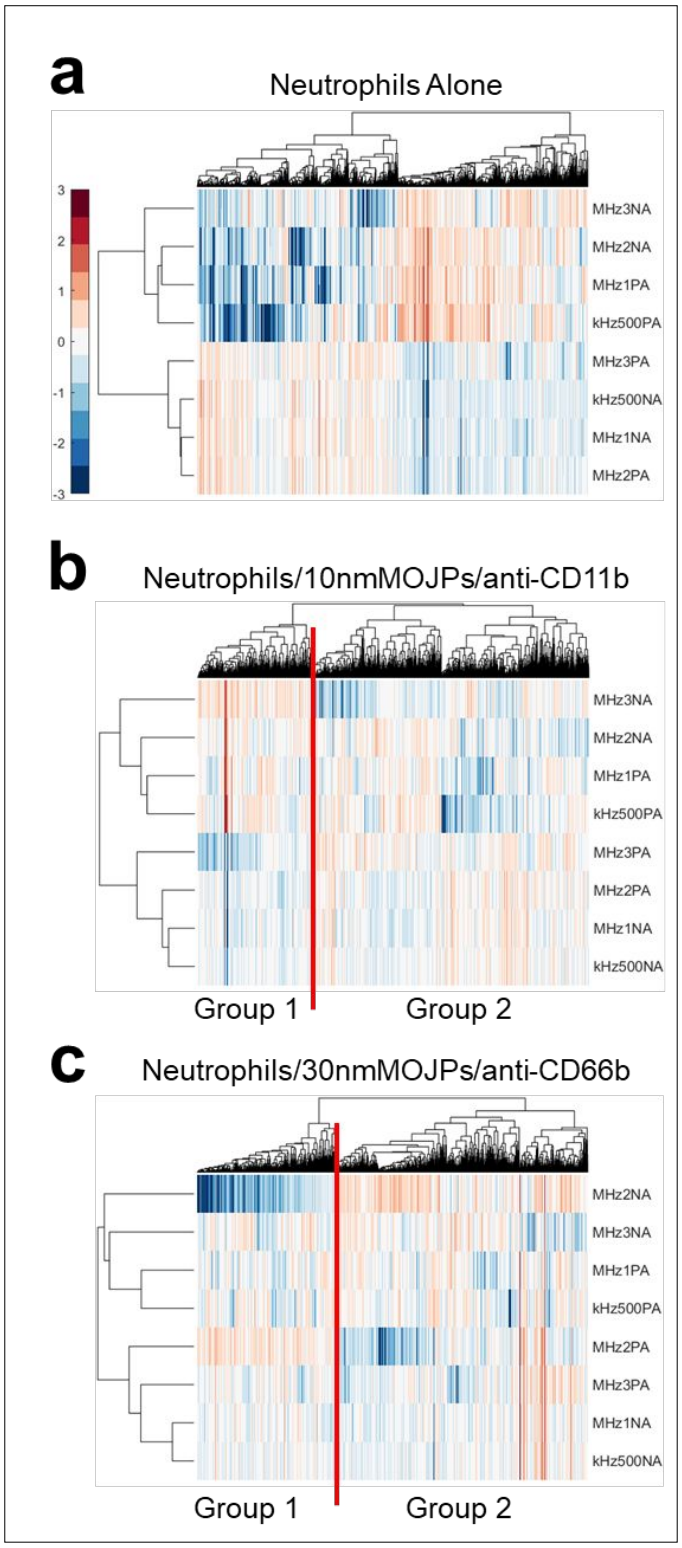

Fig. 6 Unsupervised machine learning clustering heat maps with positive (PA) and negative (NA) amplitude data measured for each voltage frequency (500 kHz, 1 MHz, 2 MHz, and 3 MHz) and for different samples. a) Sample of isolated neutrophils without any functionalized aluminum oxide-coated Janus particles (MOJPs). b) Sample of isolated neutrophils with 10 nm MOJPs functionalized with anti-CD11b receptors. c) Sample of isolated neutrophils with 30 nm MOJPs functionalized with anti-CD66b receptors. Data points are log normalized (red is variance greater than average, blue is variance less than average). Red lines indicate highest degree separation between two groups which are isolated for future classification studies as hypothesized cell-particle conjugation quantifications

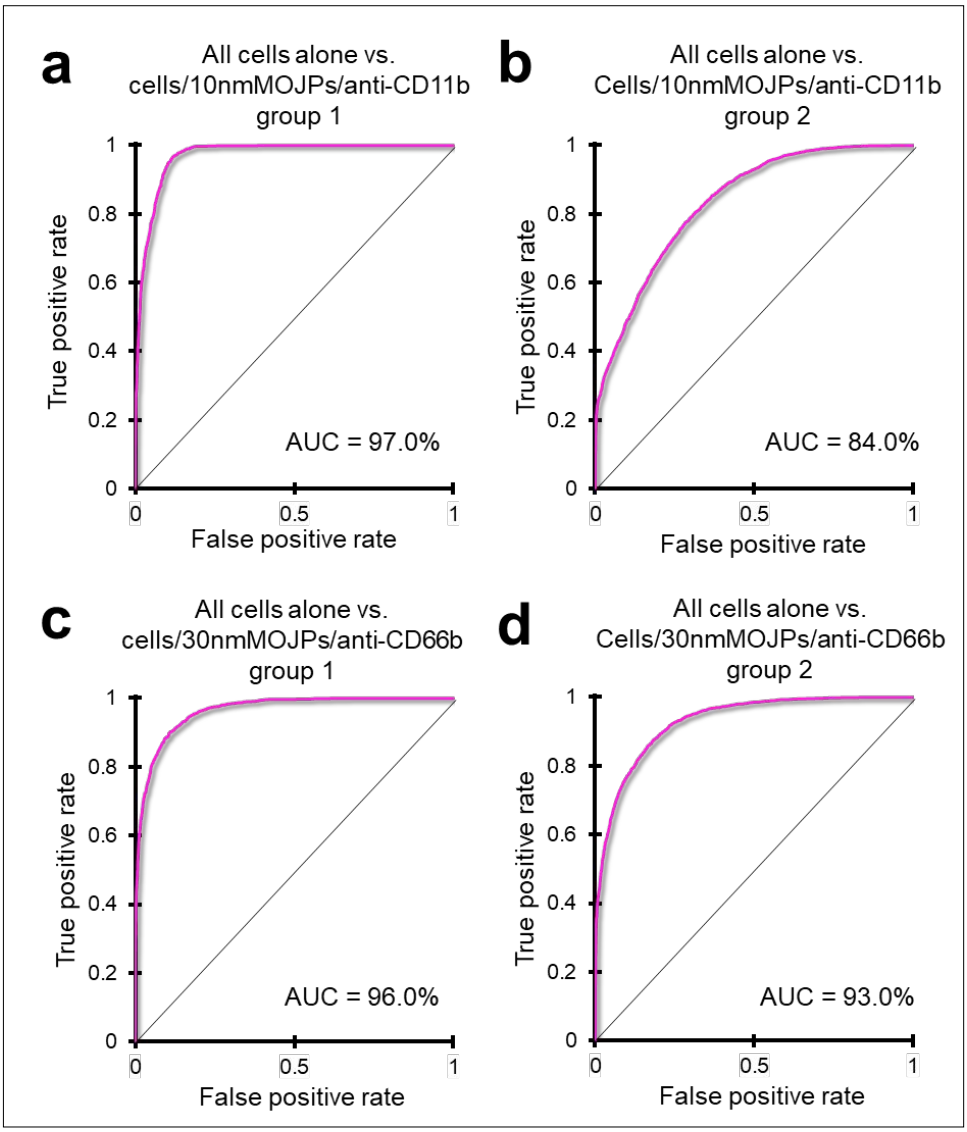

Fig. 7 Receiver operating curves classifying multifrequency impedance cytometry pulse data after potentially separating conjugated groups through unsupervised machine learning. Comparing all measured isolated neutrophils (All Cells Alone) data to neutrophils combined with 10 nm aluminum oxide coated Janus microparticles (MOJPs) functionalized with anti-CD11b antibodies (Cells/10nmMOJP/anti-CD11b) separated into two distinct groups through unsupervised clustering: a) Group 1 (potentially cell-particle conjugate data and expressing CD11b) and b) Group 2 (potentially cells which did not express CD11b). Cells Alone versus neutrophils combined with 30 nm MOJPs functionalized with anti-CD66b antibodies (Cells/30nmMOJP/anti-CD66b) separated into two distinct groups through unsupervised clustering: c) Group 1 (potentially cell-particle conjugate data and expressing CD66b) and d) Group 2 (potentially cells which did not express CD66b). For group determination, see Fig. 6